Fault Isolation of an Electro-Mechanical Linear Actuator

Matt Kemp[1], and Eric J. Martin[2]

[1,2] *Monterey Bay Aquarium Research Institute, Moss Landing, CA, 95039, USA*
mkemp@mbari.org
emartin@mbari.org

ABSTRACT

We derive a physics-based model of nominal and faulty operation for an electro-mechanical linear actuator, and use it to perform fault isolation. We present a method to identify model parameters directly from actuator performance measurements, and demonstrate the approach on an unmanned underwater vehicle mass-shifter. Our findings are twofold: first, that the system is well-represented by the model, and second, that the algorithm successfully isolated the faults.

1. INTRODUCTION

Unmanned underwater vehicles generally use electro-mechanical actuators to perform flight control tasks – e.g. thruster, elevator, rudder, mass-shifter, variable buoyancy system, etc. – (Webb, Simonetti, & Jones, 2001; von Alt, 2003; Wernli, 2000). Model-based fault detection was discussed extensively in (Gertler, 1998; Patton, Frank, & Clark, 1989). Moseler and Isermann applied it to fault detection of DC motors (Moseler & Isermann, 2000). Nandi et al. extended this to condition monitoring (Nandi, Li, & Toliyat, 2006). More recently, Fagogenis et al. (Fagogenis, De Carolis, & Lane, 2016) used a Bayesian model with a hidden switch variable to detect partial loss of thrust.

Kemp et al. (Kemp & Raanan, 2017) applied a steady-state data-centric fault-detection approach on an electro-mechanical linear actuator – a mass-shifter. The method was subsequently extended with success to a thruster (Kemp, 2017). However, the method failed when applied to rudders and elevators. Unlike thrusters and mass-shifters, which have a well-defined operating point, rudders and elevators are in a constant state of change.

One of the difficulties extending Kemp et al.'s approach (Kemp & Raanan, 2017) to fault isolation can be illustrated with an overload fault: when an obstacle stands in the way, the servo-controller increases current until the obstacle is overcome – or until overload-protection circuitry shuts the system down. Because the current is higher than usual, fault-detection is straightforward. However, because of the time-dependence, the decision boundary is unnecessarily large. We observed similar limitations with a coupling fault, where the motor and the mass become kinematically decoupled and the gap between the two increases with time.

This paper presents a model-based approach to fault-isolation of a linear actuator, and its specialization to a mass-shifter. The paper is organized as follows. Section 2 describes the electro-mechanical linear actuator model. Section 3 describes the parameter identification procedure. Section 4 presents the fault-isolation results. Section 5 discusses the results, and Section 6 summarizes the paper.

2. MODEL

2.1. System Description

The system under consideration is a mass-shifter, an electro-mechanical linear actuator that functions to move a large mass - the vehicle battery – back-and-forth in order to adjust the pitch of the vehicle. The mass-shifter under consideration consists of a DC brushed motor with a planetary gear connected to a large mass through a lead screw. The servo-controller normally operates in constant velocity mode, using position feedback from a quadrature encoder.

The motor shaft is connected to the load through a drive-train: a gear box which matches the motor's torque to the load's, a torque coupler which absorbs misalignments between the output shaft and the load, a lead-screw which converts rotation into linear motion, and a nut which connects the lead-screw and the mass.

The mass is constrained to move along parallel rails on four wheels – front and back, left and right. At either extremity, the rails are terminated by hard travel limits – blocks of aluminum designed to stop the wheels.

The mass-shifter has two modes of failure. The first is a current overload: because mass position is estimated from the motor encoder, and because the travel limit protection is

implemented in software, wheel slippage, encoder noise, or back-driving can each cause a shift in the position estimate; when this occurs, the limit protection is no longer effective. The second mode of failure is a loss of coupling, which occurs when the set-screw connecting the lead-screw to the nut comes loose. Unlike the overload failure, coupling failures occur suddenly.

To capture both nominal and faulty dynamics, we represent the system with three state variables:

$$X = \begin{bmatrix} \omega & \phi & \Delta \end{bmatrix} \tag{1}$$

where ω is the motor's angular velocity (in radians/s), ϕ is the motor's angular position (in radians), and $\Delta \equiv \phi - Dx$, the gap between motor and mass position (in radians), where x is mass position, and where the kinematic ratio D is such that Δ is zero in nominal conditions.

2.2. Electrical Model

The model for a DC electrical motor is a voltage source V_s in series with a source resistance R_s, a motor resistance R_m, an inductance L, and a back-emf voltage that is proportional to the motor's angular velocity:

$$V_s = Ri + L\frac{di}{dt} + K_m\omega \tag{2}$$

where R is the sum of the two resistances and K_m is the motor torque constant.

Most DC motors are controlled by a cascaded controller, where the inner loop controls current and the outer loop controls motor velocity. In position mode, the vehicle application issues a commanded position x_{cmd}, which is converted into a commanded velocity profile. We consider a trapezoidal profile, i.e. a constant acceleration phase, followed by a constant velocity phase, and ending with constant deceleration phase. Commanded acceleration, deceleration, and velocity are typically uploaded to the controller firmware at power-up.

For efficiency reasons, the input to the motor is a PWM voltage train rather than a DC current – the implicit assumption being that the motor inductance is large enough to smooth the current. We assume this, and replace the motor equation 2 with its time-averaged version:

$$V = Ri + K_m\omega \tag{3}$$

where V is the time-averaged source voltage - equal to the PWM duty cycle times the source voltage. This is the first model equation.

2.3. Mechanical Model

The mechanical model of the motor is:

$$J\frac{d\omega}{dt} = K_m i - \tau_{load} \tag{4}$$

where J is the effective moment of inertia, which accounts for the motor shaft, the gear box, and the mass' inertia, and τ_{load} is the torque applied to the motor shaft by the load. The load has a component due to friction – motor, drive train, and mass – and one due to gravity. We assume Coulomb friction, and make the small vehicle pitch approximation:

$$\tau_{load} = A + B\theta \tag{5}$$

where A is the zero-pitch friction, B is the friction slope, and θ is the pitch of the vehicle. This is the second model equation.

2.4. Nominal Model

The nominal model consists of the electrical and mechanical models above, augmented by the dynamics introduced by the servo-controller and the effect of voltage saturation.

The outer loop uses a PI controller to command current:

$$i_{cmd} = K_p(\omega_{cmd} - \omega) + K_i \int_{t_{ref}}^{t} dt'(\omega_{cmd} - \omega) \tag{6}$$

where i_{cmd} is the commanded current, ω_{cmd} is the commanded speed, K_p and K_i are the proportional and integral gains, and where the error integral is initialized to 0 at t_{ref}. Because the inner loop responds much faster than the outer loop, to a good approximation $i = i_{cmd}$, with the caveat that the source voltage cannot exceed the supply voltage V_{max} (i.e. the PWM duty cycle cannot exceed 100%):

$$V \leq V_{max} \tag{7}$$

Combining these gives the nominal model:

$$
\begin{aligned}
&J\frac{d\omega}{dt} = K_m i - \tau_{load} \\
&\frac{d\phi}{dt} = \omega \\
&\frac{d\Delta}{dt} = 0 \\
&i = \begin{cases} i_{cmd}(\omega) & Ri_{cmd} + K_m\omega \leq V_{max} \\ \dfrac{V_{max} - K_m\omega}{R} & otherwise \end{cases} \\
&i_{cmd} \equiv K_p(\omega_{cmd} - \omega) + K_i \int_{t_{ref}}^{t} dt'(\omega_{cmd} - \omega) \\
&\tau_{load} = A + B\theta
\end{aligned} \tag{8}
$$

2.5. Current Overload Model

When contact with the travel limit occurs, the servo-controller increases the output torque in order to maintain speed. The extra torque causes both compression of the wheel and deformation of the mass assembly. Wheel compression is nonlinear due to variable contact effects and wheel composition; we model it with a quadratic dependence. Mass assembly deformation is essentially linear with motor position.

To capture these effects, let x be the coordinate of the mass along the rail, and let x_c be the position when contact is first made. The model is the same as the nominal model, except that:

$$
\begin{aligned}
&\tau_{load} = (A + B\theta) + C(x - x_c)^2 \; when \, x > x_c \\
&\frac{d\Delta}{dt} = E\omega
\end{aligned} \tag{9}
$$

where C is the stiffness constant, and when the assembly compressibility E accounts for the linear deformation of the mass assembly.

2.6. Loss of Coupling Model

After the coupling fails, ϕ and x are no longer related kinematically. Assuming that the mass-shifter is non-backdriveable, the gap between motor and mass position increases linearly, the moment of inertia decreases, and the friction is smaller and independent of vehicle pitch:

$$
\begin{aligned}
&J'\frac{d\omega}{dt} = K_m i - \tau_{load} \\
&\frac{d\phi}{dt} = \omega \\
&\frac{d\Delta}{dt} = \omega \\
&\tau_{load} = A'
\end{aligned} \tag{10}
$$

where J' and A' are the moment of inertia and zero pitch friction without the load.

3. PARAMETER IDENTIFICATION

Parameter identification is done using a combination of manufacturer data (Maxon A-max 22-110138 motor; Maxon GP 22B-110357 planetary gear head; Nook lead-screw with 1mm/rotation pitch), direct measurements, pre-set values, and model identification. Table 1 summarizes the parameters, their values, and how they were determined.

parameter	name	value	method
R_m	motor resistance	20.2Ω	manuf
K_m	torque constant	21.2mNm/A	manuf
D	kinematic ratio	5.28e5rad/m	manuf
V_{max}	supply voltage	15.1V	measure
w_{cmd}	commanded speed	410rad/s	preset
α_{cmd}	commanded accel	6e4rad/s^2	preset
K_p	proportional gain	1.1e-3 As/rad	ID
K_i	integral gain	0.45 A/rad	ID
J	moment of inertia	4.7e-7kgm^2	ID
A	zero pitch friction	4.6e-4Nm	ID
B	friction slope	2.3e-5Nm/deg	ID
R_s	source resistance	0.8Ω	ID
C	stiffness constant	85N/m	ID
E	assembly compressibility	0.48	ID
A'	decoupled friction	3.4e-4Nm	ID
J'	decoupled inertia	4.6e-7kgm^2	ID

Table 1. Model parameters.

3.1. Nominal Model Parameters

We measured motor current using a shunt resistor in-line with the motor (NI-DAQ 9227), a voltage sensors across the motor terminals (NI-DAQ 9229), and an absolute position sensor connected to the moving mass (Tensor Solutions SP1-4 sampled by NI-DAQ 9229). The measured voltage is the motor's, i.e. source voltage minus source resistance loss:

$$
V_{measured} = V - R_s * i \tag{11}
$$

Data was passed through 100 dB anti-aliasing filters at the Nyquist frequency, and sampled at 1600 samples per second at 24 bits. Time-synchronization between the channels was maintained by a National Instruments Compact-DAQ 9174 chassis.

The servo controller (AllMotion EZSV23) used a quadrature encoder to close the loop on velocity (Maxon MR-M, 32 counts per revolution).

Figures 1-3 shows motor voltage, motor current, and motor speed vs time during nominal operation. Speed was calculated from the current and voltage as:

$$\omega_{measured} = (V_{measured} - R_m * i)/K_m \quad (12)$$

Four phases were observed:

- 0-7ms: acceleration – rapid increase of the current, voltage, and speed.
- 7-50ms: voltage saturation.
- 50-300ms: stabilization
- 300ms ++: steady-state.

Different factors are active in each phase; this allows for sequential identification of the parameters.

During the saturation phase, the source voltage is constant. Accordingly, the source resistance R_s is equal to the slope of the measured voltage versus current. Because the equation of motion for ω is first order and linear, the solution is a saturated exponential:

$$\omega = \omega_o(1 - exp(-t/\tau)) \text{ where } \tau = RJ/{K_m}^2 \quad (13)$$

where ω_o is the steady-state angular velocity. This relationship allows the moment of inertia J to be derived directly from the time constant.

During the stabilization phase, the source is not saturated. The equation of motion for ω is second order and linear, i.e. it admits closed-form expressions for the oscillation frequency and decay time:

$$\begin{aligned} \tau_{decay} &= 2J/(K_m K_p) \\ \omega^2_{oscillation} &= K_m K_i/J - 1/\tau^2 \end{aligned} \quad (14)$$

allowing the proportional gain K_p to be derived from the first equation, and the integral gain K_i from the second.

During the steady-state phase, the load is proportional to current. The zero-pitch friction A and friction slope B can be found by linear regression of torque versus pitch.

3.2. Overload Model Parameters

Figure 4 shows motor current vs distance after contact with the travel limit is made ($x = 0$). As described by the overload model, the increase is nearly quadratic. The stiffness constant

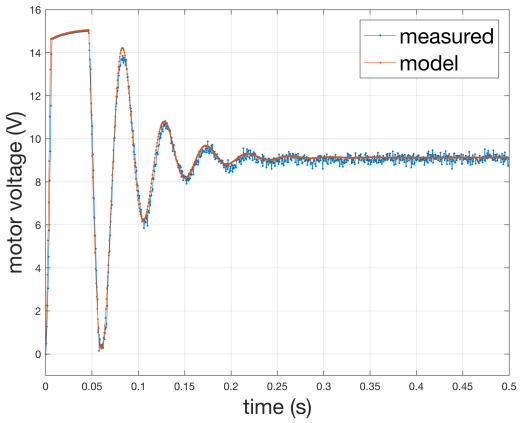

Figure 1. Motor voltage versus time.

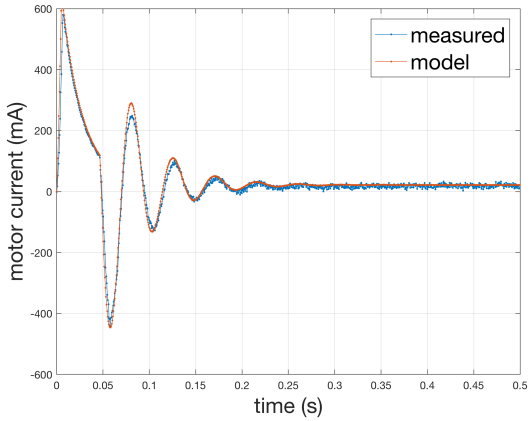

Figure 2. Motor current versus time.

C was derived by fitting the data to a quadratic model (solid line).

3.3. Coupling Fault Model Parameters

The dynamics after a coupling fault unfolds similarly as in the nominal case, the only difference being the values of A and J. A' and J' were found using the same procedure as above: J' from the voltage saturation phase, and A' from the steady-state phase.

Figure 5 shows how the gap Δ changes before and after a coupling fault. Delta was calculated by integrating motor speed (Equation 12) minus the absolute position sensor reading:

$$\Delta_{measured} = (\int_{t_{ref}}^{t} dt\omega_{measured}) - D * x_{measured} \quad (15)$$

Except for a 0.4mm of backlash, Δ is approximately zero in nominal operations. After the coupling fault, Δ increases

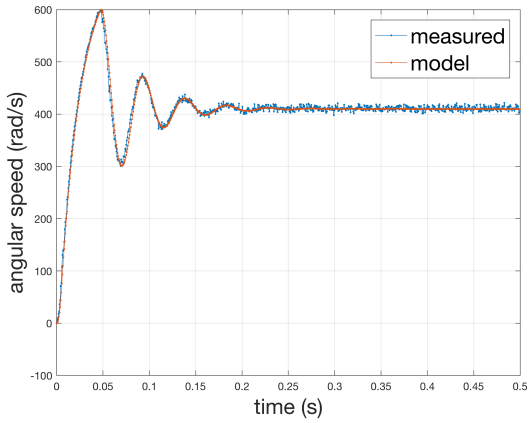

Figure 3. Motor speed versus time.

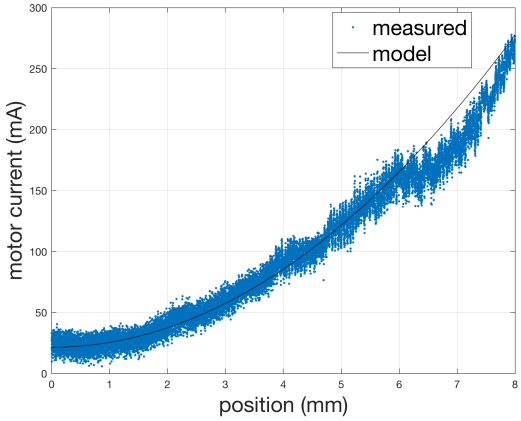

Figure 4. Current overload model.

linearly with time, reflecting the fact that the motor is turning at constant speed while the mass stays in place.

4. FAULT ISOLATION

Figures 6 and 7 show projections of the nominal and faulty data in feature space. The first figure shows the current and speed projection, and the second the delta and speed projection.

When nominal (black dots), speed and current are clustered and delta is small. This reflects the steady-state which is reached in nominal conditions.

The overload fault (blue dots) is also clustered in speed, but the current is spread across a large range. This reflects the current increase required to maintain speed. The gap Δ also increases, which combined with the fact that motor speed is maintained, indicates that substantial mechanical deformation, of order 2-3 mm, is taking place. The deformation was confirmed visually, and is reflected in the overload model.

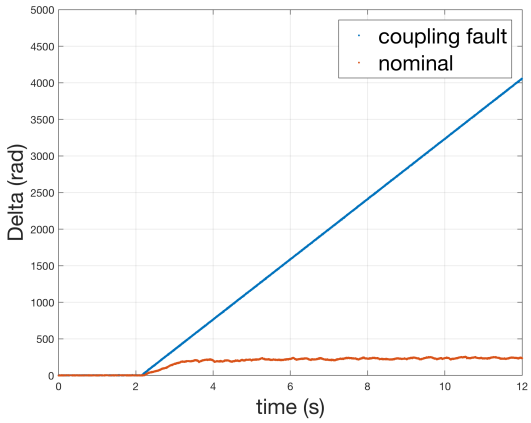

Figure 5. Delta before and after a coupling fault.

The current vs speed plot for the coupling fault is nearly indistinguishable from that in the nominal case. This is consistent with the small modification of the parameters. A much larger difference is observed in the gap Δ vs speed plot, where consistent with Figure 5, Δ increases linearly with time.

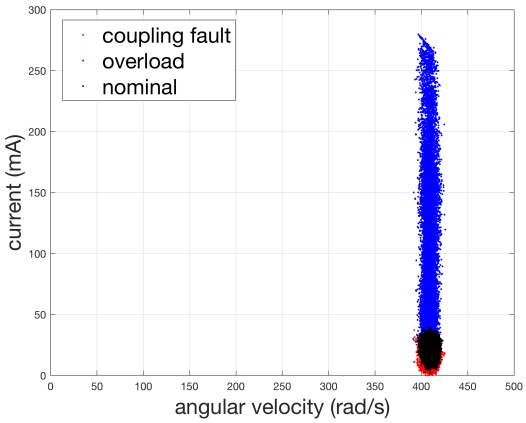

Figure 6. Current and speed in nominal and faulty conditions

4.1. Time-Dependent Mixture Model

To perform fault isolation, we represented the system as a time-dependent mixture of faulty and nominal components. The mean was computed by propagating the respective equation of motion forward in time. The variance was assumed constant. The likelihood of a component was determined by the residual between prediction and measurement.

Let $X_i(t)$ be the state predicted by model i at time t, let $Y(t)$ be the measurement, and let $H(X_i(t))$ be the predicted measurement. We computed the residual ϵ as:

$$\epsilon_i = \sqrt{[Y(t) - H(X_i(t)]^{+}\Sigma^{-1}[Y(t) - H(X_i(t))]} \quad (16)$$

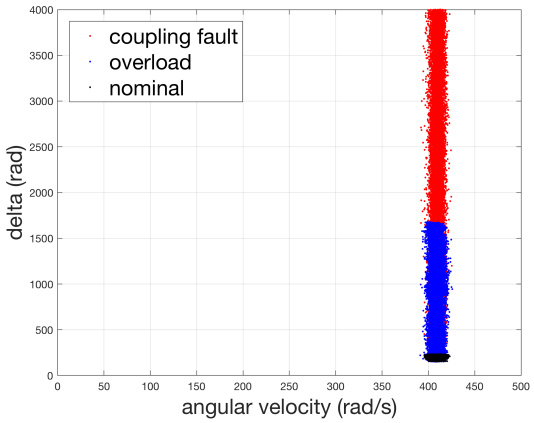

Figure 7. Delta and speed in nominal and faulty conditions

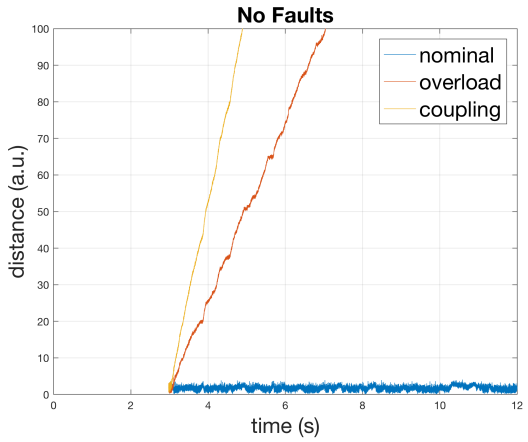

Figure 8. Fault isolation method applied to nominal data.

For simplicity, we assumed that the covariance Σ was diagonal and the same for each model.

Figures 8, 9, and 10 show the residual of each model in three cases: no faults (i.e. nominal data), overload fault, and coupling fault. In all cases, the fault was detected at t=3s.

Nominal case (Figure 8): the coupling fault model and the overload fault model both have high residuals that increase with time. For the coupling fault model, the high residual is due to its prediction of a large gap (Δ); for the overload fault model, it is due to its prediction of high current.

If one were to assume Gaussian mixtures, $P \propto \exp(-0.5\epsilon^2)$, the high values of the residuals would indicate astronomically small probabilities of either fault.

Overload fault case (Figure 9): both the nominal and the coupling fault models have high residuals. For the nominal model, this is due to its failure to explain the high current; for the coupling fault model, it is due to both its predicted high Δ and its failure to predict a high current.

The nominal and the overload models have similar residuals for about 1s after the fault is detected. This is due to a combination of factors, and will be discussed in the next section.

Coupling fault case (Figure 10: both the nominal and the overload fault models have high residuals. For the nominal model this is due to its failure to explain the large gap; for the overload fault model, it is due to both its predicted high current, and its failure to predict a large gap.

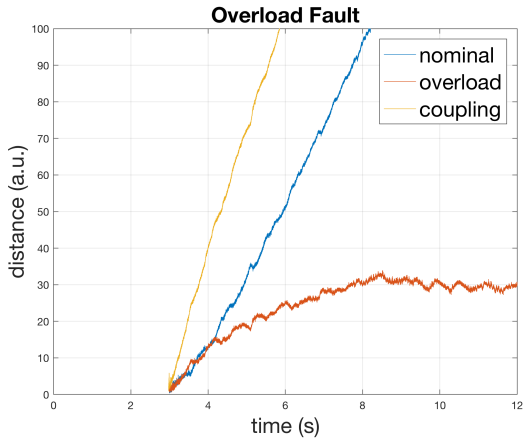

Figure 9. Fault isolation method applied to an overload fault.

5. DISCUSSION

5.1. Short Time Ambiguity

For a brief time after an overload fault, the nominal and the overload fault models have similar residuals (Figure 9). This is due to a combination of factors:

- Initialization error. When the models are invoked, they are initialized with the latest state estimate; estimation error causes artificial transient behavior.
- Variability. Variability from run to run, particularly due to small misalignments of the mass, cause absolute position sensor errors. As a result, the actual location where contact with the travel limit tab first occurs is variable.
- Detection time delay. The overload model assumes that the torque due to the travel limit is a function of the distance traveled after contact. As explained above, the location of the point of contact is uncertain. To overcome this, we made the assumption that detection is immediate, and initialized the model under the assumption that $x = x_c$ at initialization. The delay between detection and actual contact introduces a prediction error.
- Modeling error. We assumed that the force against the travel limit increases quadratically. Figure 4 shows that this is a fair but imperfect assumption.

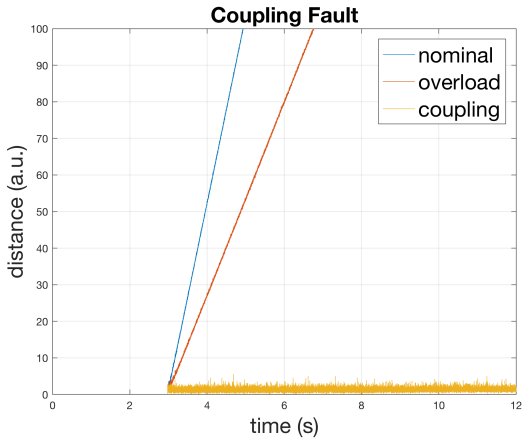

Figure 10. Fault isolation method applied to a coupling fault.

5.2. Parameter Identification

Prediction quality is a function of parameter selection. The three models are described by 16 parameter, 10 of which were derived by data fitting. The approach we followed is minimalist and partitioned, i.e. as few parameters as the physics requires, and sequential parameter identification using independent data. We believe that this procedure is robust, and that it leads to models that fit the data remarkably well. The drawbacks are that it is manual, and not adaptive.

5.3. Next Steps

We're in the process of improving the method using analytical redundancies, and of developing a hardware implementation for an autonomous vehicle:

- Current and voltage provide an estimate of angular speed; they therefore provide a redundant position estimate that can be used to isolate position sensor faults.
- The commanded current can be estimated from the time history of angular velocity, i.e. it provides a redundant current estimate.
- The quadrature encoder data currently used by the servo controller can be used as an independent position measurement.
- A strap-down system that implements this algorithm is under development for an autonomous underwater vehicle. The system is expected to undergo sea-trials in 2019.

6. CONCLUSION

We developed a model-based framework for fault-isolation of an electro-mechanical linear actuator, and tested its performance on a mass-shifter. We derived physics-based models of the system's nominal operation, of an overload fault, and of a coupling fault. We developed a sequential procedure for parameter identification, and used experimental data to populate the models. We implemented fault-isolation using a mixture of time-dependent components, whose parameters are computed from the models. We found that 1-the models accurately represented the system, and 2- that they isolated the correct faults successfully. We are in the process of adding analytical redundancies to the system, and are developing a hardware implementation for an autonomous underwater vehicle.

ACKNOWLEDGMENT

This work was done with financial support from the Packard Foundation.

REFERENCES

Fagogenis, G., De Carolis, V., & Lane, D. M. (2016). Online fault detection and model adaptations for underwater vehicles in the case of thruster failures. *IEEE International Conference on Robotics and Automation*.

Gertler, J. (1998). *Fault detection and diagnosis in engineering systems*. Marcel Dekker Editor.

Kemp, M. (2017). Actuator fault detection for uuvs. *Presentation at PHM Annual Conference*.

Kemp, M., & Raanan, B. (2017). Actuator fault detection for autonomous underwater vehicles using unsupervised learning. *Proceedings of the Annual Conference of the PHM Society*.

Moseler, O., & Isermann, R. (2000). Application of model-based fault detection to a brushless dc motor. *IEEE Transactions on Industrial Electronics*.

Nandi, S., Li, X., & Toliyat, H. (2006). Condition monitoring and fault diagnosis of electrical motors. *IEEE Transactions on Energy Conversion*.

Patton, R., Frank, P., & Clark, R. (1989). *Fault diagnosis in dynamic systems*. Prentice Hall.

von Alt, C. (2003). Remus 100 transportable mine countermeasure package. *Proceedings of Ocean 2003*.

Webb, D., Simonetti, C., & Jones, C. (2001). Slocum: an underwater glider propelled by environmental energy. *IEEE Journal of Oceanic Engineering*, *26*, 447-452.

Wernli, R. (2000). Auv commercialization - who's leading the pack. *Proceedings of Ocean 2000*.

BIOGRAPHIES

Dr. Matt Kemp is a Principal Engineer at the Monterey Bay Aquarium Research Institute in Moss Landing CA. He holds a Ph.D. in Physics from the University of North Carolina at Chapel Hill. Dr. Kemp served as Director of Concept Development with Bluefin Robotics for 5 years, and as Director of Concept Development with Nekton Research for 7 years. His research interests are unmanned underwater vehicle design and vehicle health management. He is a member of IEEE, PHM, AIAA, and AAAS.

Eric Martin is an electrical engineer at MBARI. He holds

an M.S. in Ocean Engineering from the University of Rhode Island. His research interests are ocean instrumentation, remotely operated vehicles, and virtual reality.